Chapter 2: Synthesis and Experimental Methods

The sample preparation procedure and details of different characterization techniques used for the present study are given in this chapter. The sample preparation was done by the standard arc melting furnace method. Several experimental techniques are used for the characterization, e.g., laboratory and synchrotron x-ray diffraction for structural characterization, scanning electron microscope (EVO-SEM, MA15/18, ZEISS) equipped with the energy dispersive spectroscopy (EDS) detector for the composition study, differential scanning calorimetry (DSC) for phase transition study, magnetic properties measurement system (MPMS) for magnetization measurements, and physical properties measurement system (PPMS) for magnetization and magnetotransport (magnetoresistance and Hall) measurements. The cryogenic free measurement system (CFMS) is also used for resistivity measurements. The detailed principle and procedures of these experimental methods are discussed in this chapter.

2.1 Synthesis Procedure

The samples used in the present study were prepared using the standard vacuum arc melting method, which is widely used to prepare the polycrystalline samples of intermetallic compounds and alloys. In the vacuum arc furnace, the inert atmosphere was maintained during the melting. The samples were melted in the crucible of the water-cooled copper (Cu) hearth, which acts as an anode, while the water-cooled tungsten tip acts as a cathode connected with the power supply (199 A, 18 V; INTIG-250IDS Inverter Welder). The Cu-hearth consists of 4 crucibles used to keep more than one sample for melting. The high thermal conductivity of Cu provides the uniform distribution of heat within the Cu-hearth, which prevents the melting of the particular portion of Cu-hearth. At the same time, the low work function of tungsten enables the high emission of the electron, which

facilitates the arc generation at low power. The arc is generated between the tungsten tip and Cu-hearth in the presence of argon (Ar) gas with a pressure of around one psi. A typical operating condition is 60-80 Ampere at 12 Volts. The tip shape of the tungsten cathode enables high current density at the tip. This provides plasma (or arc) formation between cathode and anode by the passage of the electrons through Ar gas to the anode. The generated arc can provide a temperature of ~3000 ºC, which is enough to melt most metallic elements. The melting procedure is given as follows.

The raw materials with a minimum of 99.99 % purity were weighted in the appropriate quantity using electronic balance from Mettler Instruments (model no. XS105). These weighted raw materials were taken in one of the Cu-crucible inside the arc furnace chamber. In addition, a titanium (Ti) ball was also taken in another Cu-crucible. After that, evacuation of the arc furnace chamber was done up to the minimum vacuum of the order of ~10^{-3} mbar by a rotary pump. Subsequently, purging was done by filling the Ar gas up to the atmospheric pressure and evacuating again. The heavy molecule of Ar gas facilitates the evacuation of air molecules from the chamber. Generally, the purging is done 4-5 times to achieve the good inert atmosphere required to prevent the oxidation of metallic materials during melting. After the purging, the Ar gas was filled up to ~1 psi, and then arc was generated by the power supply. First, the Ti was melted to further reduce the air molecules inside the arc furnace chamber as Ti is a highly reactive material and hence can easily trap the air molecules by oxidizing itself. After that, the raw materials were melted to form the sample. In general, the melting was done 3-4 times by flipping the sample to achieve a good homogeneous composition. The mass of the material was measured before and after melting. The weight loss was found to be below 1% for all the prepared samples. The button-shaped ingot (or sample), obtained after melting, was further annealed under the inert Ar

atmosphere for homogeneity. This process was done by wrapping the ingot in the Molybdenum (Mo) foil of thickness 0.025mm and sealing it inside a quartz ampoule after evacuating it upto the vacuum of ~10^{-6} mbar using a turbomolecular pump or diffusion pump and finally filling the Ar gas upto near atmospheric pressure to achieve the inert environment. The vacuum-sealed quartz ampoule was annealed in the furnace at the required temperature and hours, depending on the composition. Finally, the vacuum-sealed ingot was quenched or slowly cooled to room temperature to achieve the required ordered phase. An actual image of the arc melting furnace with the vacuum sealing setup used for sample preparation in the present study is given in Figure 2.1.

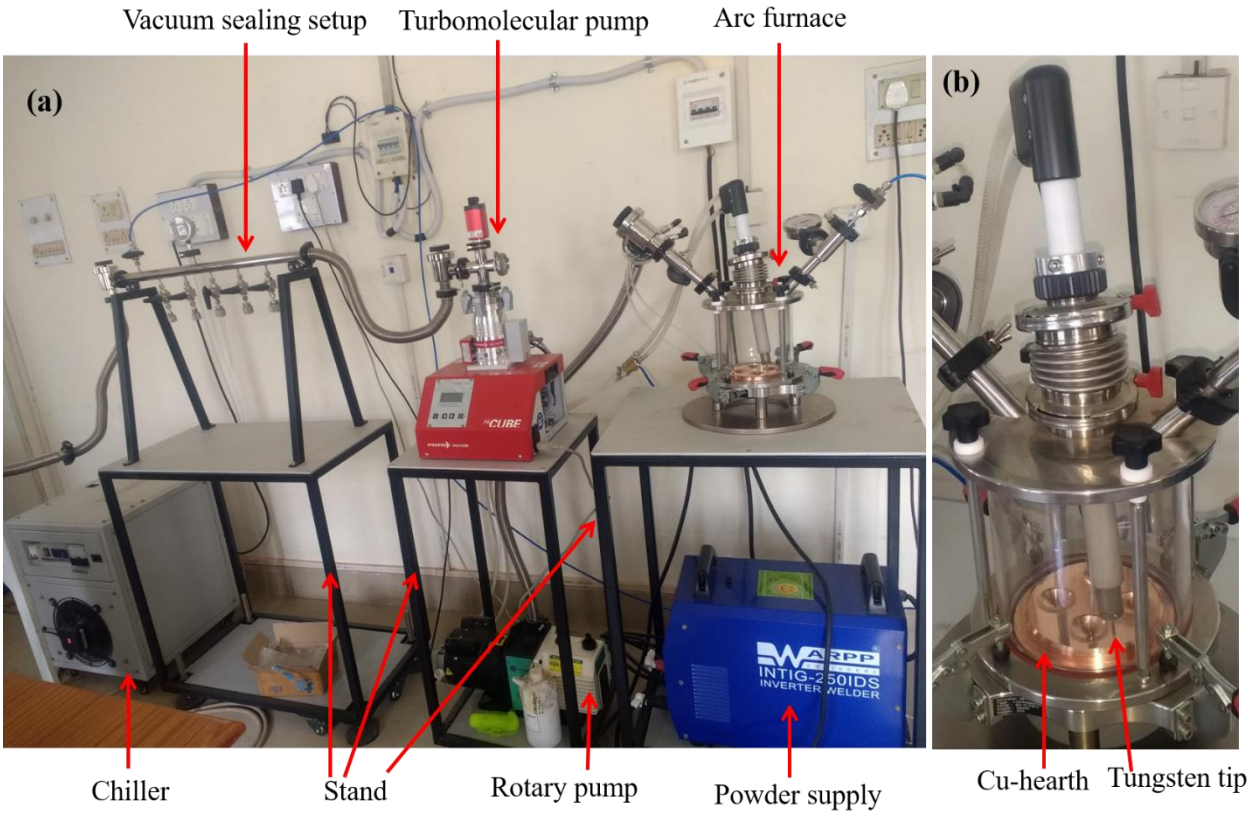

Figure 2.1: (a) Real image of sample preparation unit at the School of Materials Technology, IIT (BHU), Varanasi, India. (b) An enlarged view of the vacuum arc melting furnace.

2.2 X-ray Diffraction

The powder x-ray diffraction (XRD) is a powerful method to determine the crystal structure of the materials. The randomly oriented grains of powder sample diffract the incoming x-ray based on Bragg's law given as:

$$2d\ sin(\theta) = n\lambda \ \ldots (2.1)$$

Where, d, θ, λ and n are interplanar spacing, Bragg angle, the wavelength of x-ray, and order of reflection, respectively. The set of values of d, θ, λ, and n for which Bragg condition (eq. 2.1) satisfied, the diffraction takes place, and Bragg peak appears in the XRD pattern. In the Bragg law, the crystallographic arrangements of atoms are considered in the form of lattice planes, and the Bragg diffraction occurs via interaction between incident x-rays and lattice planes. A schematic diagram of XRD based on Bragg law is given in Figure 2.2. The diffracted x-rays are detected using detectors and provide a series of information like crystal structure, phase fraction, dimension of unit cells, crystallite size, microstrain, and so on.

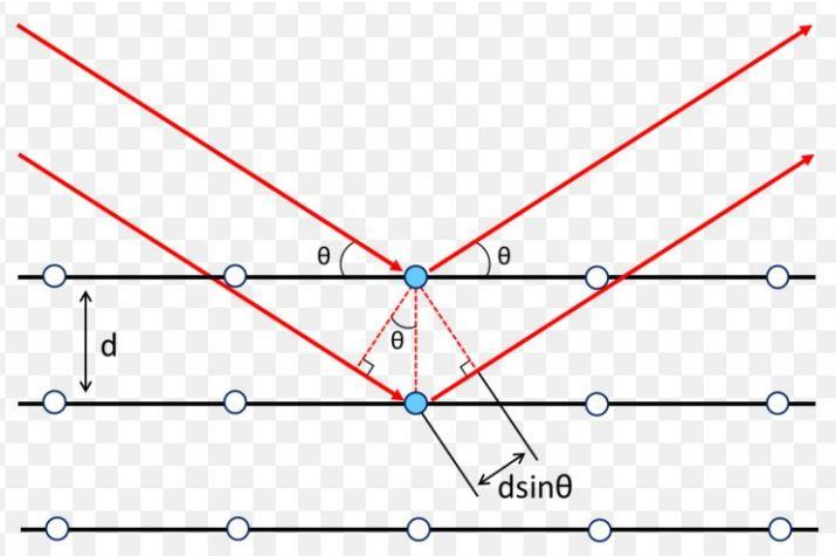

Figure 2.2: Schematic diagram of x-ray diffraction by a set of lattice planes of the crystal.

In the present study, the temperature dependent (13–300 K) laboratory XRD was collected using an 18-kW Cu rotating anode-based high-resolution x-ray diffractometer fitted with a curved graphite crystal monochromator in the diffraction beam and a closed-cycle He refrigerator-based low temperature attachment (Rigaku, model no. RINT 2500/PC series). This diffractometer works in the Bragg-Brentano geometry. A real image of this diffractometer is given in Figure 2.3.

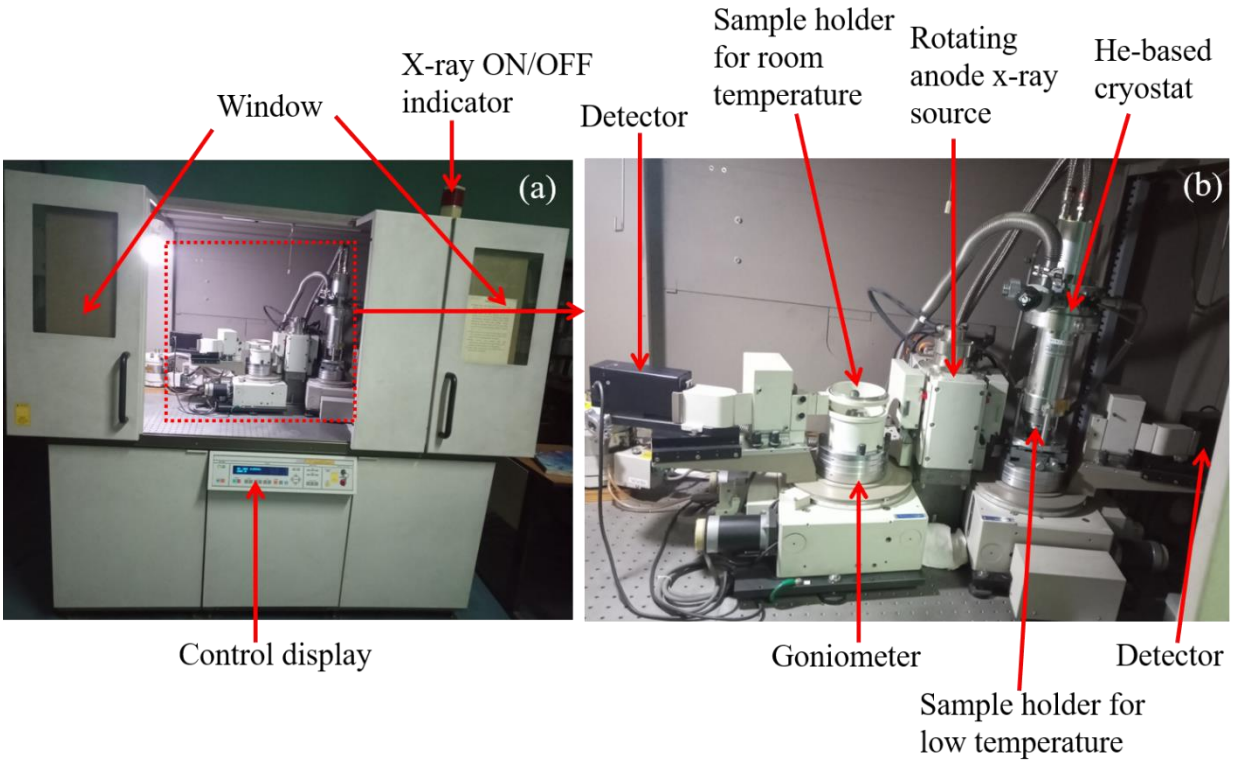

Figure 2.3: (a) A real image of temperature dependent x-ray diffractometer in the School of Materials Science and Technology, IIT (BHU). (b) An enlarged view of the machine part.

2.3 Scanning Electron Microscope and Energy Dispersive Analysis of X-rays

The chemical composition was checked by the energy dispersive analysis of x-rays (EDAX) technique. The EDAX characterization was performed using EVO-Scanning Electron Microscope MA15/18 (ZEISS) equipped with an energy dispersive spectroscopy (EDS) detector (Model No.

51N1000-EDS System). The working principle of SEM is depicted by schematic diagram in Figure 2.4, wherein the primary electrons are generated by a source that usually consists of Tungsten filament. The primary electrons are focused and guided to incident on the sample by a set of magnetic lenses. The interaction of the electron with the sample leads to the generation of secondary electrons, backscattered electrons, and characteristic x-rays. These are detected by separate detectors, namely SE, BSE, and EDS, respectively (see Figure 2.4), and provide information about sample morphology, phase contrast, and elemental composition. The working principle for EDAX in the SEM is given in Figure 2.5. The electron beam incident on the sample and interact with it by ejecting the electrons from the inner shells like the K-shell of the sample. This process leads to the creation of vacancies in the inner shells. These vacancies are filled by jumping electrons (transition) from the outer shells (L, M, N…). This transition leads to the emission of electromagnetic waves (or characteristic x-rays as wavelength lies in the range of x-ray) with definite energy depending on the transition shells involved for e.g., the transition from L to K, M to K, M to L… give K_{α}, K_{β}, L_{α}…, respectively. These characteristic x-rays are detected by the EDS detector and provide information about the proportion of elements present in the sample in the form of the energy spectrum. In the energy spectrum, the maximum intensity appears for the highest proportion element, the second most intensity appears for the second-highest proportion element, and so on.

The EDAX data were collected using the finely polished sample by scanning the different parts of the sample. Each scan was taken for a minimum of 30 seconds to achieve the correct atomic percentage of each element. The average composition was determined by taking the average of scans on different sample parts.

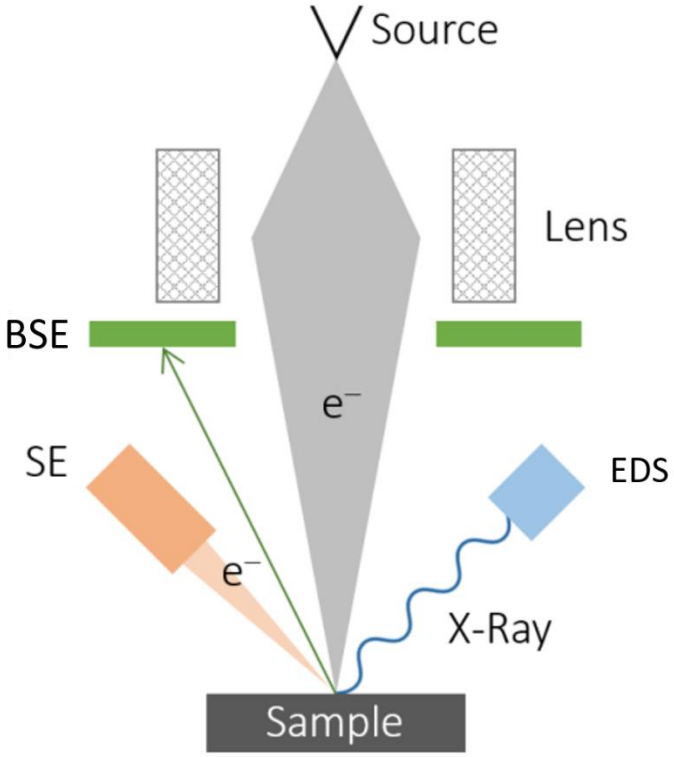

Figure 2.4: A schematic diagram of working principle of scanning electron microscope [236].

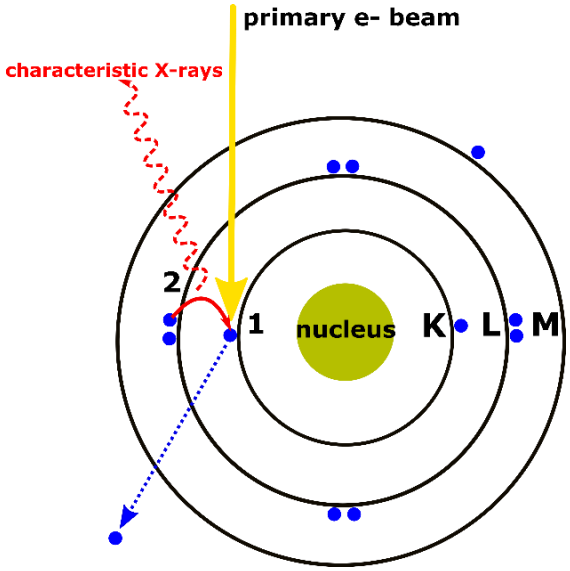

Figure 2.5: A schematic mechanism of characteristic x-rays emission from inner shells of an atom by primary electron beam [237].

On the other hand, the backscattered electron (BSE) images were also recorded, which provides information about phase homogeneity as the different contrast observed in the BSE image for different phases present in the sample.

2.4 Differential Scanning Calorimetry

The differential scanning calorimetry (DSC) characterization is used to measure crystalline phase transition temperature, latent heat during phase transition, specific heat or heat capacity, the heat of fusion, glass transition temperature, and so on. The basic principle involved in DSC is the difference in the amount of heat required to increase the temperature of a sample, and a reference material is measured as a function of temperature as depicted in Figure 2.6. The sample and reference are heated together at the same temperature using heaters. The whole process is automated and controlled by a computer using the software. In the present study, the DSC measurement was performed during heating and cooling cycles using DSC-60 plus (Mettler, M/s Shimadzu Pte Ltd.) in dynamic mode. The heating and cooling rate was maintained at 10 ºC/minute in the temperature range of -50 to 300 ºC. For the DSC measurement, first of all, the data for two blank platinum crucibles/pans were collected to prevent the abnormal signal in the measurement. Subsequently, a few mg of samples was taken in one pan, and the second pan was considered as a reference pan, and then measurement was carried out as depicted in Figure 2.6. The contribution of the blank pan was subtracted, and the data from the sample was obtained. The sample was maintained in the nitrogen gas environment during the DSC measurements.

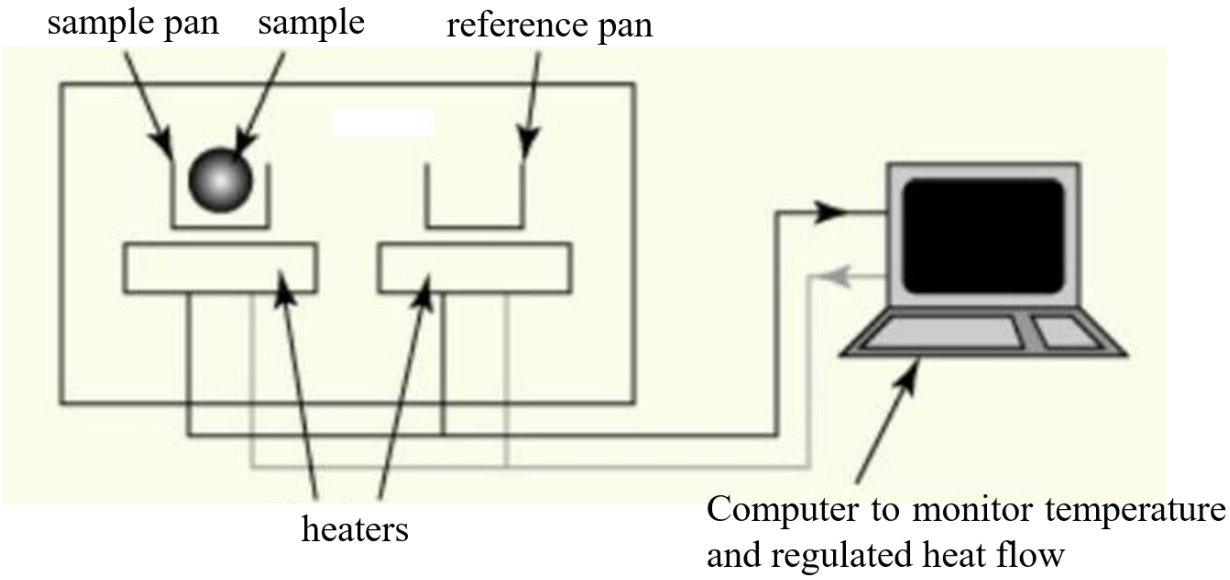

Figure 2.6: A schematic diagram of the working principle of DSC [238].

2.5 Magnetic Measurements

The temperature and field-dependent magnetization (*M(T)* and *M(H)*), as well as ac-susceptibility ($\chi(T)$ and $\chi(H)$) measurements, were performed using physical properties measurement system (PPMS, Quantum Design) and magnetic properties measurement system (MPMS, Quantum Design), which contain superconducting quantum interference device (SQUID) with vibrating sample magnetometer (VSM). In the PPMS, the VSM option was employed for *M(T)* and *M(H)* measurements in the 2 to 400 K temperature range and -9 T to 9 T (produced by solenoid-based superconducting magnet) magnetic field range, respectively. The schematic operating principle of the VSM option is shown in Figure 2.7. In the VSM, the sample oscillates near a detection or pickup coil in the uniform magnetic field. This oscillation induces a voltage in the pickup coil due to a change in magnetic flux as per Faraday's law. This time-dependent induced voltage in the pickup coil (V_{coil}) can be expressed as:

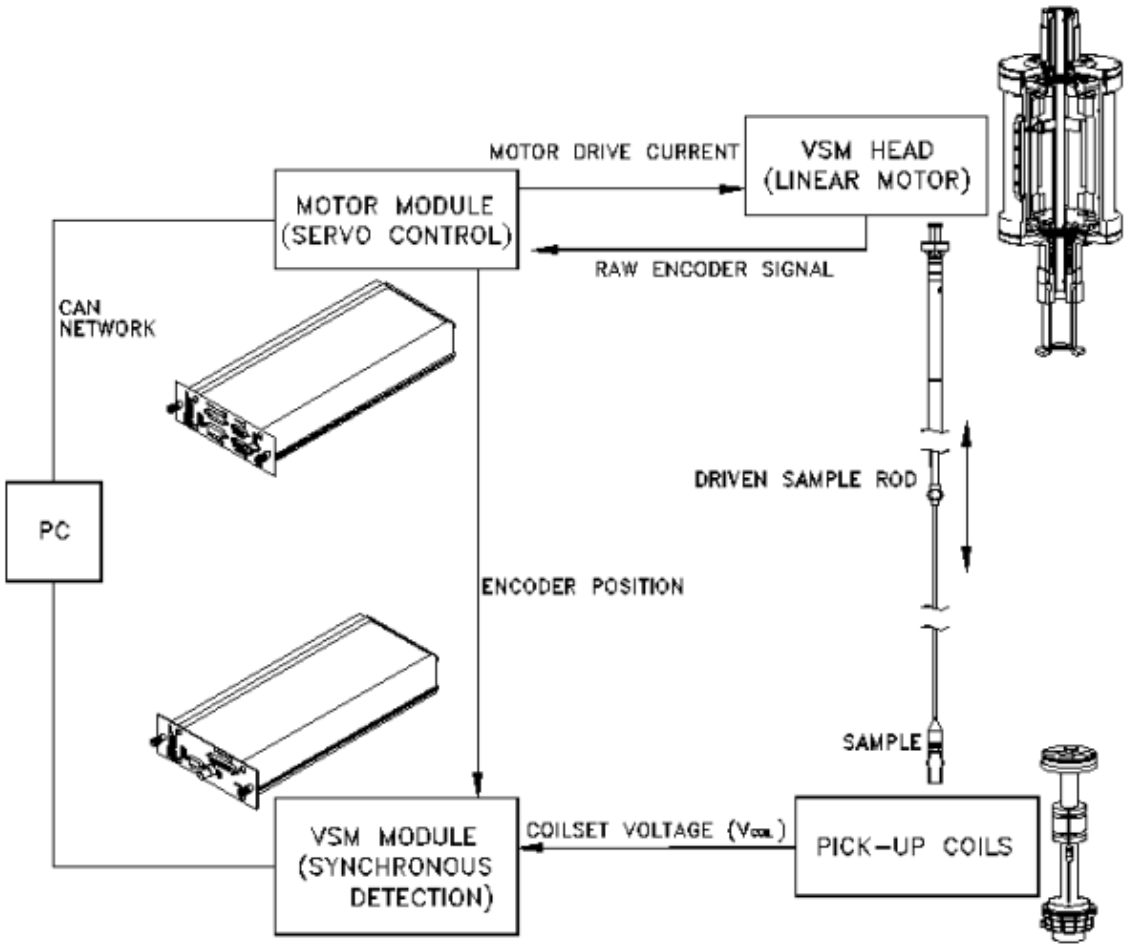

Figure 2.7: A schematic diagram of the operating principle for the VSM option of PPMS [239].

$$V_{coil} = \frac{d\phi}{dt} = \left(\frac{d\phi}{dz}\right)\left(\frac{dz}{dt}\right) \ldots (2.2),$$

where, ϕ, t, and z are magnetic flux enclosed in the pickup coil, time, and vertical position of the sample, respectively. For a sinusoidal oscillation of the sample, the pickup voltage can be expressed as [239]:

$$V_{coil} = 2\pi f C m A \sin(2\pi f t) \ldots (2.3),$$

where, *f, C, m,* and *A* are oscillating frequency, coupling constant, dc magnetic moment of the sample, amplitude of oscillation, respectively. This induced voltage is detected by the pickup coil and amplified for further acquisition. The VSM option consists of a linear motor (head) for vibrating the sample, a coilset puck for detection, electronics to operate the linear motor, and detecting the response from the pickup coils, as depicted in Figure 2.7. These are automated and controlled by MultiVu software. The VSM has the sensitivity of $<10^{-6}$ emu, i.e., it is able to resolve magnetization changes of less than 10^{-6} emu. A typical operating condition is 2 mm peak amplitude and 40 Hz oscillating frequency.

In the PPMS, the AC measurement system (ACMS II) option was used for $\chi(T)$ and $\chi(H)$ measurements in the 2 to 400 K temperature range and -1 T to 1T field range, respectively. In the ac magnetic measurements, a small ac drive field is superimposed on the dc field develops time-dependent magnetization in the sample. This time-dependent magnetization enables change in the magnetic flux enclosed in the pickup coil and hence induces a voltage in the pickup coil without the motion of the sample. Despite the superposition of the ac drive field and dc field, there may be phase lag, especially at the higher frequencies. Thus, ac magnetic measurement provides information of ac-susceptibility (χ) as well as phase shift (Φ). Therefore, it is possible to speculate in-phase (or real) component (χ') and out-phase (or imaginary) component (χ'') [240]. They can be quantified as $\chi' = \chi cos\Phi$ and $\chi'' = \chi sin\Phi$, where χ is defined by the ratio of the amplitude of the change in the magnetic moment with the amplitude of change in the ac field, i.e., $\chi = dM/dH$. The ac magnetic measurements provide information about the dynamics of the magnetic moments of the sample. In general,χ is measured in a three-point measurements process that utilizes the calibration coils to enhance the accuracy of the measurement. In the three-point measurements process, the first and second data are collected with the sample positioned at the center of the

bottom detection coil and top detection coil, respectively. At last, the third is collected with sample positioning back at the center of the bottom detection coil. The three-point measurement provides the comparison of the sum of the two bottom coil signals with the two times of the top coil signal. This helps to correct for drifts of the sample moment and background over the course of the measurement. A schematic diagram of the ACMS II coil set is shown in Figure 2.8, wherein different coil sets are indicated. The ac drive amplitude and frequency were optimized for every measurement.

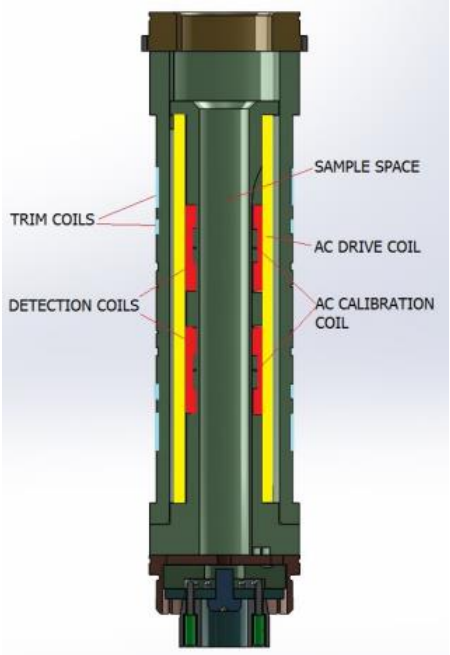

Figure 2.8: A schematic diagram of ACMS II coil set [240], where different coils are indicated.

SQUID-MPMS with VSM: The superconducting quantum interference device (SQUID) based MPMS is a very sensitive magnetometer wherein SQUID coil enables to detection of even a subtle magnetic field in the living organisms. The liquid He cooled SQUID measures changes in magnetic flux when VSM moves the sample through the superconducting detection coil. The SQUID

consists of two superconductors separated by thin insulating layers to form two parallel Josephson junctions, as depicted in Figure 2.9. The basic working principle is that a constant biasing current is maintained in the SQUID device, and the measured voltage oscillates with the changes in phase at the two Josephson junctions. This depends upon the change in the magnetic flux. When the sample oscillates through the SQUID device using VSM, the change in flux leads to a change in voltage, which is measured.

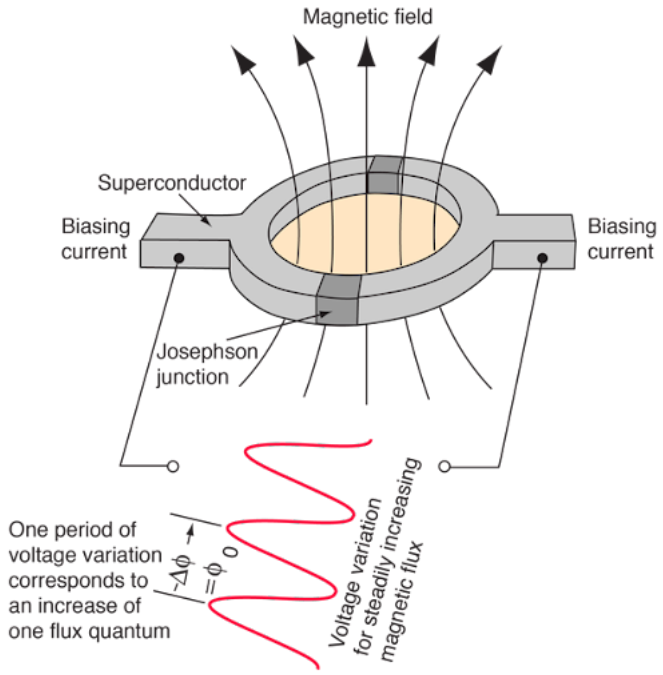

Figure 2.9: The schematic diagram of magnetic flux detection by SQUID, where $\Delta\phi$ is the change in flux and ϕ_0 is flux quanta [241].

2.6 Magnetoresistance and Hall Measurements

The Electrical Transport Option **(**ETO) equipped with PPMS was employed for magnetotransport (magnetoresistance and Hall) measurements using the four-probe method in the 2–400 K temperature range and -5 T to 5 T field range. In the ETO, there are two separate channels. Each

channel contains its separate electronics, consisting of a high precision current source and voltage preamplifiers coupled to a Digital Signal Processor (DSP) [242]. This enables the resistance measurement of two different samples simultaneously. The rectangular-shaped sample was mounted on the sample puck with four electrical contacts (two for current and two voltage measurements). The beauty of the four-probe is that the resistance of contact, leads, and wire is eliminated due to the large input impedance of the voltmeter. For longitudinal voltage measurement, collinear contacts are made, as depicted in Figure 2.10(a). In contrast, for the transverse Hall voltage measurement, the contact for voltage measurement was made perpendicular to the applied current, as depicted in Figure 2.10(b). The sinusoidal ac current source with 20 mA current, 18.3 Hz frequency, and averaging time of 5 seconds was used for the measurements.

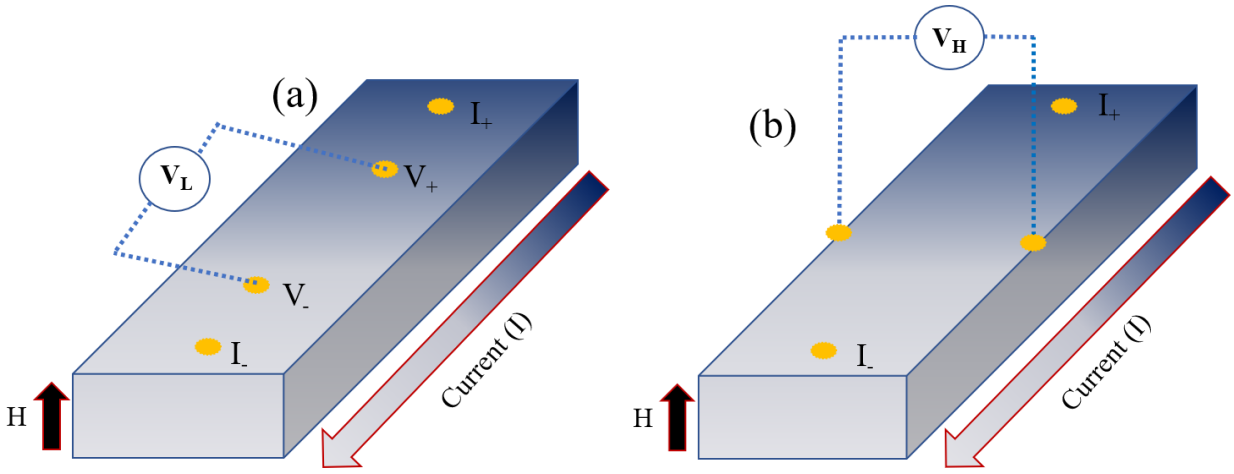

Figure 2.10: A typical schematic diagram of (a) Longitudinal voltage and (b) Hall (transverse) voltage measurement setup, where I_+, I_-, V_+, and V_-, indicate positive current, negative current, positive potential, and negative potential contacts respectively while H, V_L, and V_H represent the magnetic field, longitudinal voltage, and Hall voltage, respectively.

The resistivity was calculated using the formula $\rho = R\frac{A}{L}$, where R, A, and L are resistance, cross-sectional area, and distance between voltage contact, respectively. The Hall and longitudinal resistivity were measured by sweeping the magnetic field from +5 T to -5 T at the fixed temperatures. A real image of a sample mounted using ETO of PPMS for magnetotransport measurements is depicted in Figure 2.11, wherein Kapton tape was used for insulating the sample from the substance while copper wires were employed for making connections.

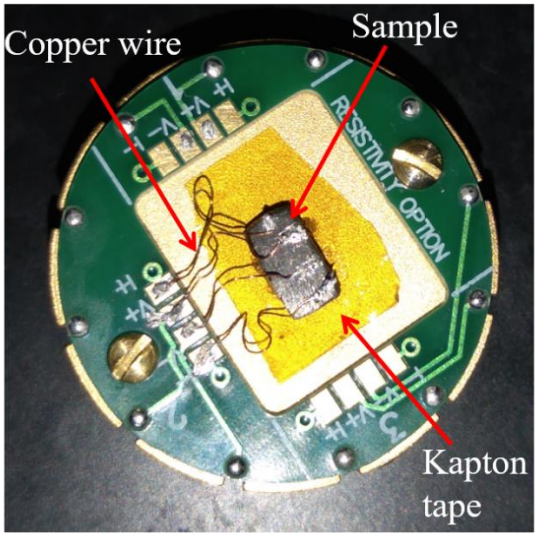

Figure 2.11: A real image of a sample mounted for magnetotransport measurements using the four-probe method in ETO of PPMS at School of Materials Science and Technology, IIT (BHU).

In the present thesis, a few resistivity measurements under magnetic field were also carried out using a cryogenic free measurement system (CFMS). The CFMS provides the variable temperature insert in the range of 3–300 K and magnetic field in the range of -5 T to 5 T by superconducting solenoid magnet. All the systems were automated and controlled by the computer using LabVIEW software. The real image of the CFMS system is shown in Figure 2.12. The rectangular-shaped sample was employed for measurement based on the four-probe method. The current source

(model No. 228A VOLTAGE/CURRENT SOURCE) and the nanovoltmeter (model No. 181 NANOVOLTMETER) supplied by the KEITHLEY instruments were employed for the measurement. The sample was fixed on the sample holder using GE Varnish (see Figure 2.13). The connections on the sample were made by soldering the copper wire using pure indium as a flux because indium has a low melting point, which prevents the metallic sample from oxidation during soldering. A self-made connection between the sample and the current source as well as the nanovoltmeter was designed using the sample insert for the measurement. The measurement was carried out by taking the 5 to 9 times average by applying the dc current of 100 mA in the positive and negative direction (i.e., $\pm I$) to remove the offset voltage in the sample. The current source and voltmeter were switched on at least 1 to 2 hours before starting the measurement in order to warm them to minimize the possibility of random signals/noise during the measurement.

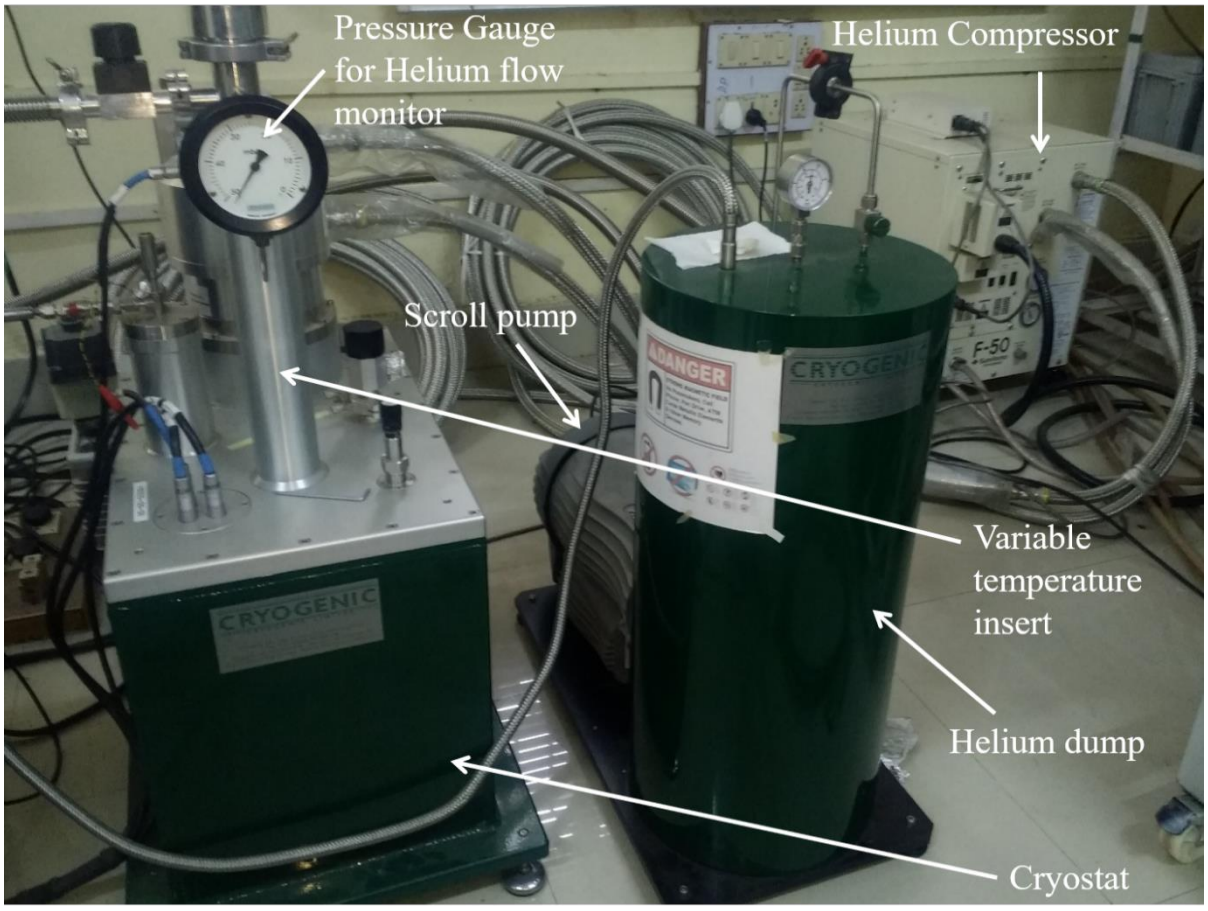

Figure 2.12: The real image of CFMS setup at School of Materials Science and Technology, IIT (BHU).

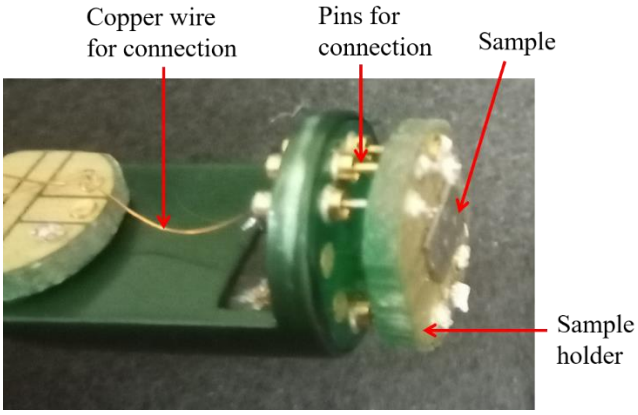

Figure 2.13: The real image of sample holder for magnetoresistance measurement using CFMS at School of Materials Science and Technology, IIT (BHU).

2.7 Synchrotron X-ray Powder Diffraction

In the present thesis, the advanced synchrotron-based light source has been extensively used to carry out synchrotron x-ray powder diffraction (SXRPD) measurements in order to capture the small features/changes in the crystal structure. The synchrotron produces high-intensity beams of light more than a million times brighter than the sunlight [243]. The synchrotron beam is produced when high-energy electrons are forced to travel in a circular orbit inside tunnels by the application of the magnetic field [244]. It is based on the concept of emission of electromagnetic radiation by accelerated charge, i.e., when a charged particle (say electron) changes its direction, it emits electromagnetic radiation or light [244]. The synchrotron x-rays are produced when the electron moves faster enough so that the wavelength of emitted light lies in the order of the x-ray region on changing its direction. The synchrotron-based x-ray source has several advantages over laboratory-based x-ray sources in the form of high energy, high brilliance, wide energy spectrum, tunability of wavelength, highly polarized, and emitted in very short pulses [244]. Thus, SXRPD provides high-resolution, high signal-to-noise ratio and bulk information of the samples compared to the laboratory-based XRD. This enables to characterize the structure of materials in much depth using a synchrotron-based x-ray source.

There are different components involved in generating the synchrotron-based x-rays, as depicted by a schematic diagram in Figure 2.14. These components are Linac, Booster ring, Storage ring, and Beamlines, which are discussed below [244].

2.7.1 Linac

In the Linac, an electron gun (E-gun) produces the electrons, similar to the cathode ray tube found in television. These emitted electrons are accelerated to high energy (~MeV) using high potential differences.

2.7.2 Booster Ring

The high-energy electrons from the Linac are injected in a booster ring, wherein electrons are further accelerated to huge energy (~GeV). In the booster ring, electrons travel nearly at the speed of light. The booster ring runs a few times in a day only for a few minutes when the storage ring requires refilling.

2.7.3 Storage Ring

The highly energetic electrons from the booster ring are finally injected into the larger storage ring for several hours at very low pressure (~10^{-10} mbar). In the storage ring, electrons are turned or deflected by a series of bending magnets or undulators, which leads to x-ray emission, i.e., when the highly energetic electrons are deflected, they lose their energy which is emitted in the form of electromagnetic radiation or synchrotron radiation. In general, synchrotron radiation contains infrared (IR) to x-rays spectrum, which can be extracted as per requirements.

2.7.4 Beamlines

The emitted x-rays are guided to the experimental hutch through beamlines to characterize the materials. The beamlines contain a series of mirrors, monochromators, slits, focusing devices to achieve precisely required x-ray beam spot on the sample for the characterization.

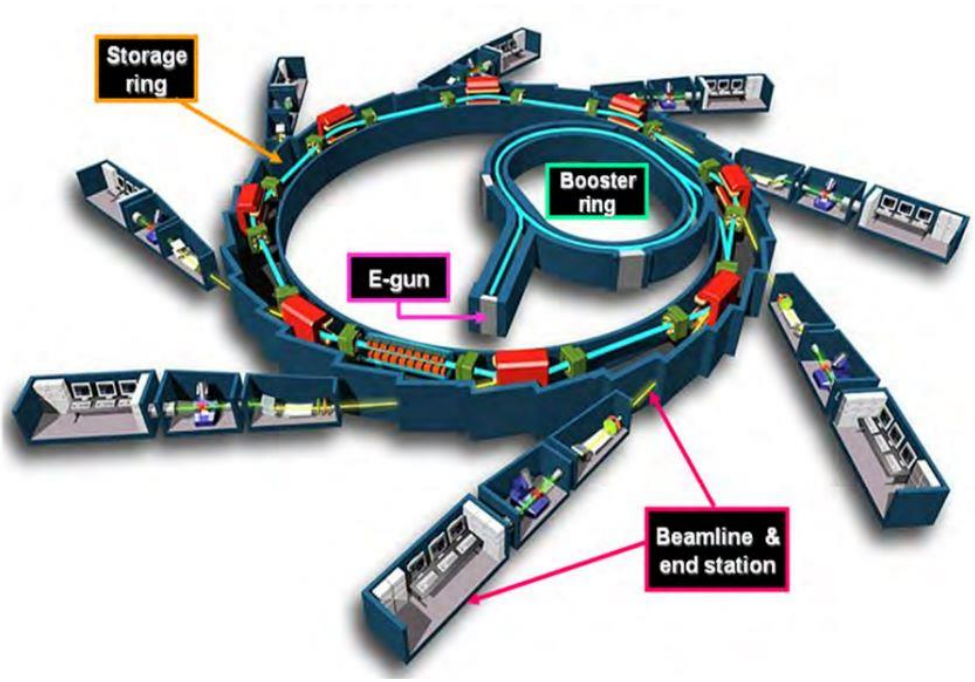

Figure 2.14: A schematic diagram of synchrotron light source and beamlines [245].

In the present study, two different synchrotron light sources, namely PETRA-III and ELETTRA, were employed for the SXRPD measurements. The details of the measurement procedure and used beamlines are discussed below.

2.7.5 P02.1 Beamline of PETRA-III

In the present study, the temperature dependent SXRPD pattern were collected using high energy (60 keV) x-rays with wavelength $\lambda \sim 0.207$ Å at P02.1 beamline of PETRA-III, DESY, Hamburg, Germany [246]. The schematic diagram of the P02.1 beamline of PETRA-III is given in Figure 2.15 (a), wherein the path of x-ray from undulator to detector via specimen/sample is depicted.

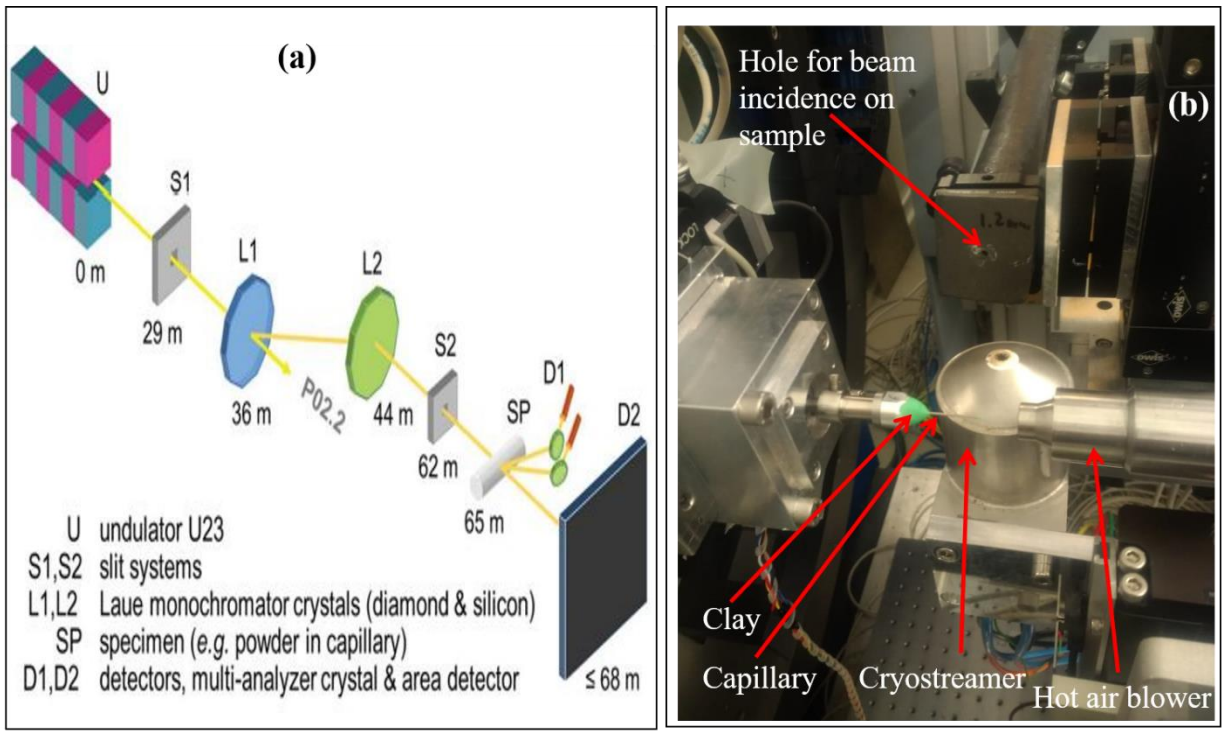

Figure 2.15: (a) Schematic diagram of optics of P02.1 beamline of PETRA-III, DESY [246]. (b) Real image of mounted capillary during measurement at P02.1 beamline of PETRA-III, DESY.

For the SXRPD measurements, borosilicate capillaries were used as sample containers. The fine powder sample was packed in the borosilicate capillaries, spinning continuously during measurement to minimize the texturing effect in the SXRPD data. A real image of mounted capillary ready for diffraction measurement at the P02.1 beamline of PETRA-III is given in Figure 2.15 (b). The SXRPD data was collected in the transmission mode based on the Debye-Scherrer principle using a 2D detector (Perkin Elmer, 200×200 μm^2 pixel size). The high-resolution SXRPD data were collected by moving the 2D detector away from the sample (sample to detector distance (SDD) ~ 1200-1500 mm), while the high-*Q* pair distribution function (PDF) data were collected by moving the 2D detector close to the sample (SDD ~ 200-400 mm) to capture higher angle Debye cones. The high-*Q* data for empty borosilicate capillary were also collected to remove the

background contribution required to get diffraction data only from the sample. For the temperature variation (100-400 K), a nitrogen cryosteamer was used directly to the capillary. The raw 2D image data were integrated into 1D diffraction (Intensity vs 2θ) using the program Fit2D and Dawn-Diamond.

2.7.6 Xpress Beamline of ELETTRA

The SXRPD pattern with pressure was collected using high energy (25 keV) x-rays with $\lambda \sim 0.495$ Å at Xpress beamline of ELETTRA, Trieste, Italy [247]. The high-resolution SXRPD was collected up to 14 GPa using membrane-driven diamond anvil cell (DAC) for generating the pressure. The methanol-ethanol mixture in 4:1 ratio was employed for the pressure transmitting medium. The pressure was monitored by the ruby fluorescence method wherein a few tiny ruby chips (~5–10 μm) were included along with the powder samples in the DAC pressure chamber. A schematic diagram of DAC is shown in Figure 2.16(a), wherein the location of different components is depicted. The real image of the experimental hutch and ruby fluorescence setup at the Xpress beamline of ELETTRA is shown in Figure 2.16(b) and (c), respectively. The inset above Figure 2.16(c) depicts the automation of the pressure membrane system.

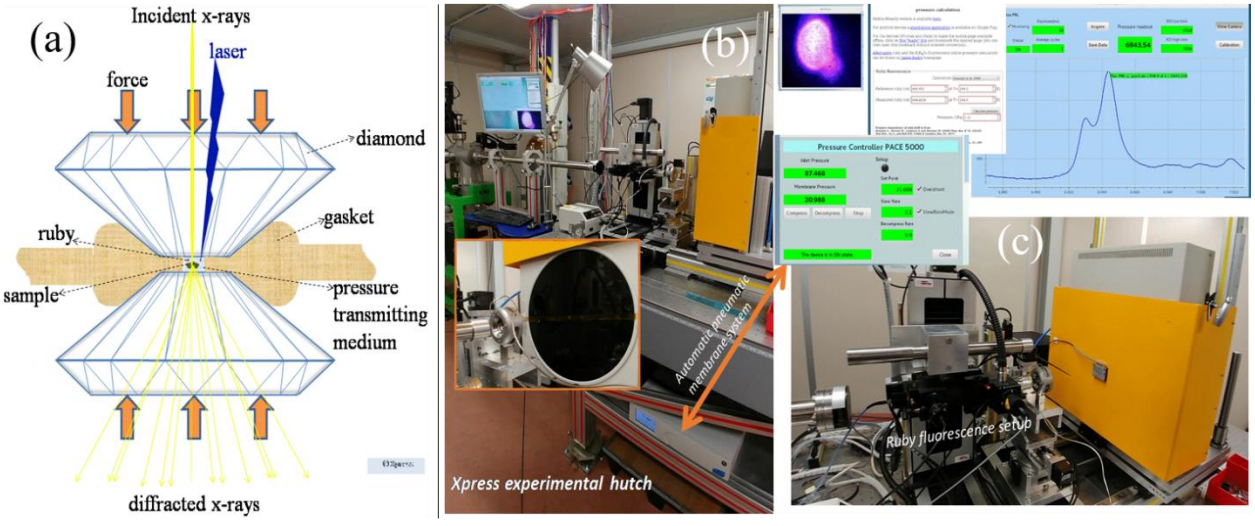

Figure 2.16: (a) Schematic diagram of diamond anvil cell (DAC). The (b) and (c) show the real image of the experimental hutch and ruby fluorescence setup at the Xpress beamline of ELETTRA. The inset above (c) depicts the automation of the pressure membrane system.